ARTICLE OPEN

Madden–Julian Oscillation-induced extreme rainfalls constrained by global warming mitigation

Shijing Liang[1], Dashan Wang [1✉], Alan D. Ziegler [2], Laurent Z. X. Li[3] and Zhenzhong Zeng [1✉]

The sixth assessment report of the IPCC indicates low-to-high confidence in trends of extreme rainfall with regional inconsistency in the tropics, where a key phenomenon causing intra-seasonal variations in weather is the Madden–Julian Oscillation (MJO). It remains unknown how the MJO-induced extreme rainfall and the societal exposure may change in response to global warming and climate mitigation attempts. Here, using eight CMIP6 models that capture the eastward-propagating MJO structure and amplitude, we detect a nearly 60% increase in extreme rainfall over tropical Asia and Australia by the end of the 21st century under the fossil-fueled warming scenario (SSP5-8.5); 84% of this change is associated with MJO-induced extreme rainfall. Extreme rainfall increases are modulated by the warming-induced asymmetric changes in MJO phase characteristics, occurring mostly over the lands with distinct zonal differences. The region that is most likely to be affected includes Malaysia, Indonesia, and northern Australia where 96.68 million people and 9.72 million km^2 of urban areas are exposed to potential danger stemming from extreme rainfall. More than 95% (99%) of the population (urban) exposure can be potentially avoided under the "middle of the road" development (SSP2-4.5) scenario, whereby CO_2 emissions hover around current levels before starting to fall mid-century.

INTRODUCTION

Nearly 300 million people worldwide are exposed to annual floods, causing more than US$651 billion loss per year over the past two decades[1]. Flooding triggered by extreme rainfall is particularly frequent and destructive in low-lying and rapidly developing tropical regions of Asia and Oceania. The vulnerability of the region to extreme precipitation was on display in December 2020 when widespread flooding impacted southern Thailand and Indonesia, killing at least 34 people, damaging 587,100 residential houses, and causing 60 million USD economic loss[2]. More than 25 major floods or severe weather events causing substantial damage were reported in Southeast Asia and tropical Oceania in the boreal winter season (months from November to April) of 2020 (ref. [2]). The recently released sixth assessment report (AR6, ref. [3]) emphasized that extreme precipitation will likely increase in the tropics under continued global warming, but with consider-able regional inconsistency, as well as uncertainty pertaining to the mechanisms triggering extreme rainfall[4–6]. Meanwhile, the Paris Agreement aims to reach a net-zero greenhouse gas emission target and limit warming below 2 °C of pre-industrial levels[7]. Uncertainties exist whether the implementation of global climate mitigation strategies, mainly initiated by mid-latitude countries, will have an effect on vulnerable regions of the tropics where future extreme rainfall is projected to impact greater populations and cause increased levels of damage owing to acceleration in the global hydrological cycle[1,8].

The most important triggering mechanism associated with extreme rainfall at intra-seasonal scale over tropical Asia and northern Australia is the Madden–Julian Oscillation[9,10], which is the several-thousand-km envelope of clouds, winds, and rainfall that moves eastwards along the equator with a 20–90 day timescale during the boreal winter season[11] (Supplementary Fig. 1). The MJO induces precipitation anomalies within alternating regions of enhanced and suppressed convection[12,13]. Extreme rainfall events may occur when the MJO is in an enhanced convective state that affects weather not only in its immediate geographical location but in areas leading and trailing its path[14–16]. In addition, the MJO affects extratropical regions through exciting Rossby waves, leading to the far-reached MJO teleconnections in the North Pacific and North Atlantic[17,18].

Many studies have made projections on changes in MJO activity in a warming climate via Earth System Models (ESMs)[13,19–21], but it remains unclear how changes in MJO-induced extreme rainfall may influence the societal exposure in response to future warming and climate mitigation attempts[22]. Such efforts rely on accurate simulation of MJO processes in ESMs. However, most CMIP5 models largely underestimate MJO amplitude and fail to reproduce a coherent eastward propagation of MJO[23]. Recently, some CMIP6 ESMs have demonstrated substantial improvements in simulating the structure of MJO mainly due to the reasonable simulation of horizontal moisture advection over the Maritime Continent of tropical Southeast Asia[24]. These model advances create an opportunity to address the dynamics of MJO-related extreme rainfall and its potential socio-economic consequences in the coming decades.

Here, using climate model outputs for various global warming scenarios, we investigate projected changes in the MJO contribu-tion to regional extreme rainfall, along with associated changes in the exposure of population and urban areas in tropical Southeast Asia and northern Australia to extreme precipitation during the boreal winter seasons when MJO is the most enhanced[11,12]. First, we compare historical-simulation outputs of selected CMIP6 models with fields derived from reanalysis data and precipitation observations to evaluate the capability and accuracy of the ensemble simulations in capturing MJO structure and associated precipitation (Supplementary Tables 1, 2; Supplementary Figs. 2–7;

[1]School of Environmental Science and Engineering, Southern University of Science and Technology, Shenzhen, China. [2]Faculty of Fisheries Technology and Aquatic Resources, Maejo University, Chiang Mai, Thailand. [3]Laboratoire de Météorologie Dynamique, Centre National de la Recherche Scientifique, Sorbonne Université, Ecole Normale Supérieure, Ecole Polytechnique, Paris, France. ✉email: wangds6@sustech.edu.cn; zengzz@sustech.edu.cn

details see "Methods"). We then analyze the projected changes in MJO-induced precipitation extremes by the end of the 21st century under the fossil-fueled development Shared Socioeconomic Pathway (SSP5-8.5) scenario, focusing on geographical variability in particular. The mechanisms of extreme rainfall changes were explored by identifying the asymmetric changes in MJO phase characteristics, including the changes of occurrence and amplitude of each MJO phase. This asymmetry implies the existence of uneven changes during different stages of MJO movements, resulting in varying patterns of MJO-induced extreme rainfall changes across different phases. Finally, we assess the extent that SSP2-4.5 (the historical trends of development) and the SSP1-2.6 (the green road) scenarios may limit increases in MJO-associated extreme rainfall and the concomitant effects on exposure. Unless stated otherwise, all references to rainfall changes are for the boreal winter.

RESULTS

MJO-induced extreme rainfall is amplified under warming

For the historical period (1994–2014), the multi-model average boreal winter total rainfall is 900.4 mm over the study area, varying greatly from 211.7 mm in Mainland Southeast Asia to 1849.9 mm in the Maritime Continent, with northern Australia (620.4 mm) and the Philippines (906.6 mm) being intermediate (Supplementary Table 3). MJO-induced rainfall comprises 59–66% of the total rainfall in the four sub-regions. Similarly, the regional variations of extreme rainfall match those of total rainfall, but with MJO-induced extremes making up lower proportions (47–53%) of the total extreme rainfall (Supplementary Table 3).

Under the most intense warming scenario (SSP5-8.5), projected total rainfall increases by 103.3 mm (11%) across the region by the end of the 21st century, but in different regional proportions (Table 1). The increase is the largest for the Maritime Continent (176.6 mm). Smaller amounts are projected for Mainland Southeast Asia (36.8 mm), the Philippines (53.2 mm), and northern Australia (75.2 mm). Most or all of the increased rainfall is associated with MJO, as the proportions of non-MJO-induced rainfall in some areas decrease. For example, the projected increase in MJO-induced rainfall over the Maritime Continent is higher than the increase in total rainfall (282.2 versus 176.6 mm, Table 1), representing a decrease in predicted non-MJO-induced rainfall in the future.

An increase in total rainfall may not necessarily lead to negative impacts, but extreme rainfall often does[25,26]. Of concern is that the majority of the increase in total rainfall is attributed to an increase in extreme rainfall (Table 1). The areal mean increment of extreme rainfall is 103.9 mm and accounts for nearly 60% of the historical level, even higher than the increase in total rainfall (103.3 mm). The projected increase in extreme rainfall is particularly high in the Maritime Continent (245.9 mm); secondary in northern Australia

(55.9 mm). Comparable to the changes in total rainfall, most of the increases in extreme rainfall are also associated with MJO. For example, the projected increase in MJO-induced extreme rainfall comprises 64, 74, 68, and 101% of the projected increase in total extreme rainfall in the Maritime Continent, the Philippines, Mainland Southeast Asia, and northern Australia, respectively (Table 1). The MJO proportion in the projected extreme rainfall increase is higher compared to the historical period (Supplementary Table 3). Overall, 84% of the increases in extreme rainfall across the study region are associated with active MJO, demonstrating the important role of the MJO in the projected increase of extreme rainfall in a warming future.

Spatially, most of the increased extreme rainfall, including that associated with the MJO, concentrates on land areas (Fig. 1a, b), particularly within the Maritime Continent (including Malaysia, Indonesia, Papua New Guinea, and Singapore). The changing patterns of MJO-induced boreal winter total rainfall and extreme rainfall frequency are also comparable with patterns of the projected total change (Supplementary Figs. 8a, b, 9), further illustrating the vital role of MJO in influencing rainfall (especially extremes) in a warmer climate. Over time, both MJO-induced extreme rainfall and boreal winter extreme rainfall are projected to increase rapidly and significantly (two-sided t-test, $p < 0.01$) compared to the historical period (Fig. 1c). On average, extreme rainfall over their region is predicted to increase at a rate of 18.5 mm per decade after 2015, while the trend is smaller for MJO-induced extreme rainfall (15.6 mm per decade). Consistent with simulation results[27], little change is projected before 2039 (Supplementary Figs. 10, 11). After 2039, the models present high consistency with increases in extreme rainfall. Further, the increasing rate is accelerated at the end of the 21st century. For the periods of 2039–2059 and 2079–2099, the projected rates of increase in MJO-induced extreme rainfall are 11.6 and 31.0 mm per decade, respectively.

Increments in MJO-induced extreme rainfall potentially will trigger societal impacts. For the Maritime Continent, a striking increase of extreme rainfall exceeding the 5-year return value threshold is predicted to occur in locations where 93.85 million people now reside, covering an area of 9.40 million km² (Table 1). In other regions, the population (urban area) exposure is 2.76 million (0.23 km²) for Mainland Southeast Asia and 0.06 million (0.09 km²) for northern Australia. Regionally, based on population density, the largest impact zone is concentrated in the west of the Maritime Continent, particularly Surabaya in the eastern part of Java, Indonesia (Fig. 1d). Several highly urbanized and densely populated cities, such as Kuala Lumpur in the south of the Malay Peninsula, Bandung and Jakarta in the west of Java Island, are also likely to be exposed to the increase in MJO-induced extreme rainfall (Fig. 1d). New Guinea is projected to be exposed to the largest increase in MJO-induced extreme rainfall, but the population density is relatively low (Fig. 1d). In northern Australia,

Table 1. Projected changes in boreal winter rainfall and extreme rainfall under the SSP5-8.5 scenario and the exposure of population and urban area to the increment of MJO-induced extreme rainfall.

| | Boreal winter rainfall increases | | | Boreal winter extreme rainfall increases | | | Exposure | |
	Total (mm)	MJO (mm)	MJO/total (%)	Total (mm)	MJO (mm)	MJO/total (%)	Population (million persons)	Urban areas (million km²)
All	103.3	153.5	149	103.9	87.3	84	96.68	9.72
Maritime Continent	176.6	282.2	160	245.9	157.8	64	93.85	9.40
Philippines	53.2	94.7	178	49.2	36.3	74	0	0
Mainland Southeast Asia	36.8	43.2	117	31.7	21.7	68	2.76	0.23
Northern Australia	75.2	114.5	152	55.9	56.7	101	0.06	0.09

The exposure is estimated using the extreme rainfall threshold of the 5-year return value based on the current distribution of population and urban areas.
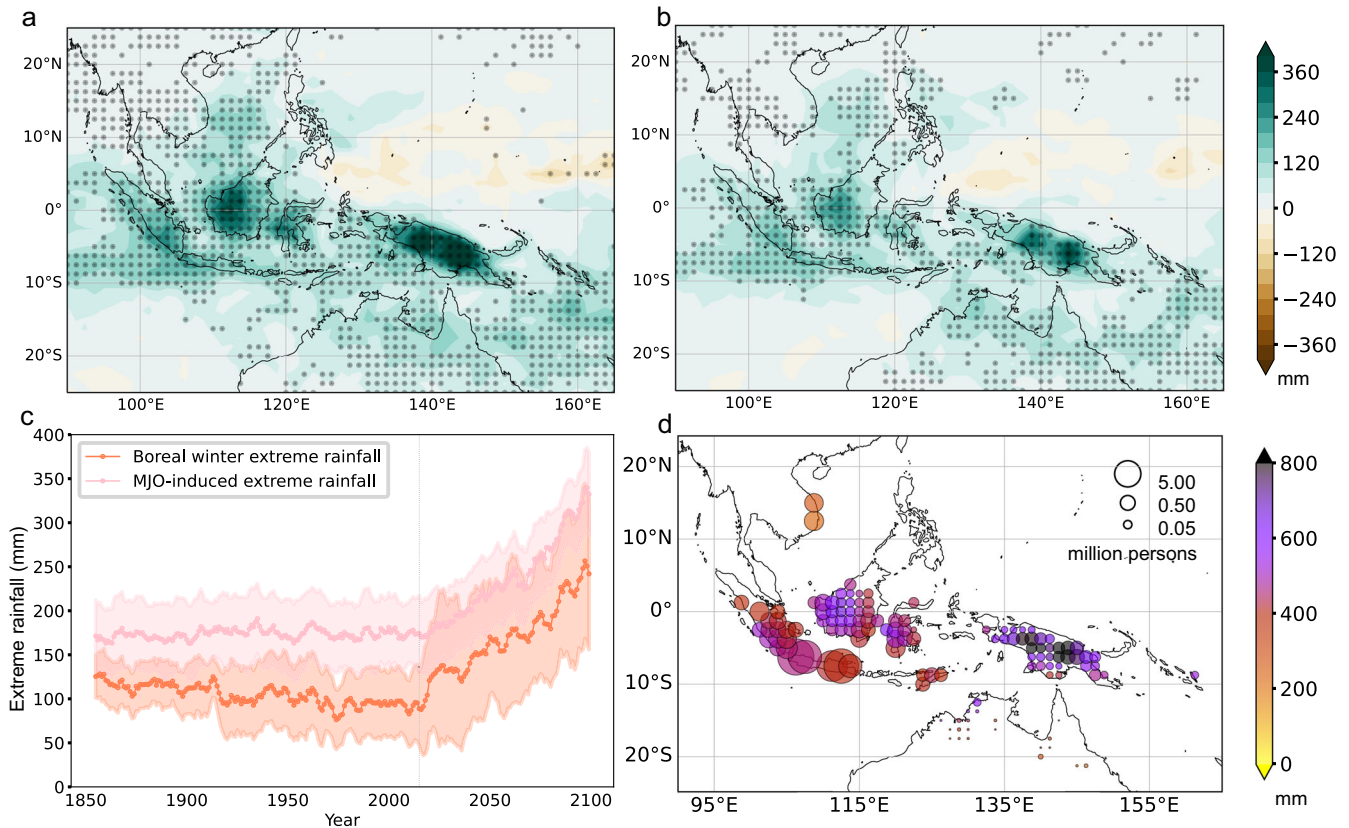
Fig. 1 Spatiotemporal changes of multi-model mean boreal winter extreme rainfall under the SSP5-8.5 scenario. Spatial distribution of the changes in boreal winter extreme rainfall amount (**a**) and MJO-induced extreme rainfall amount (**b**) between the future period (2079–2099) and the present period (2015–2035) under the SSP5-8.5 scenario over the study area. Stippling denotes where the multi-model mean changes exceed the inter-model variance. **c** Temporal series of the boreal winter extreme rainfall and MJO-induced extreme rainfall over the land areas within 25°S–20°N, 95°E–155°E during 1855-2099. Values are smoothed through the 5-year running mean. Shadings refer to half of the inter-model spread. **d** Exposure map of population to the projected increases of future MJO-induced extreme rainfall. The future MJO-induced extreme rainfall is the simulated increments between the future (2079–2099) and present (2015–2035) periods added up to the historical period (1994–2014). The size of the circles represents the amount of exposed population, while the color shows the MJO-induced extreme rainfall amount.

the highest risks to MJO-induced extreme rainfall increment would mainly be located near Darwin. Notably, due to anticipated growth in the rates of population and urbanization[28], the area and the total number of people affected by these projected changes would almost certainly be higher. In addition, many of these areas contain agricultural lands and infrastructure that would also be affected by extreme rainfall.

MJO phase changes modulate extreme rainfall increments

Substantial attention has been given to how anthropogenic warming may affect the MJO-associated genesis and it influence on rainfall-associated impacts in the future[19–22]. Two aspects of the MJO are relevant: (1) the MJO characteristics (i.e., amplitude and frequency of active states); and (2) its geographic location in reference to the eight "phases" that operationally described MJO movement[29–32] (Fig. 2 and Supplementary Fig. 1). An increase in MJO activity would be fundamentally boosted by thermodynamic and dynamic processes that favor larger moist-static energy, increased lower-level atmospheric instability, enhancement of deep convection heating, and re-enforcement of perturbations and convergence[21,22,33,34]. Consistent with theoretical considerations, positive trends are indicated for the MJO occurrence and amplitude in all eight phases for the aggressive SSP5-8.5 warming scenario (see "Methods"); however, the projected increased activity is not uniformly distributed (Supplementary Fig. 13). For example, projected increases in MJO occurrence are nearly two

days in phases 2, 5, and 6, while only slight changes are indicated for other phases. The increases in MJO amplitude are more substantial, demonstrating significant enhancement (Wald test, $p < 0.05$) for all but phases 3 and 7. Compared with the previous studies[35,36], discrepancies occur in MJO phases 2, 4, and 7. We found increases in MJO increases in MJO occurrence for phase 2, while the changes are slight for phases 4 and 7. However, we find consistency in that the MJO occurrence and amplitude tend to increase under warming when MJO enhances convection over Maritime Continent and west Pacific.

Projected changes in MJO phase characteristics and MJO-phase-composite rainfall extremes are tethered[19,22,37]. Multi-model simulations consistently predict that amplified convection associated with MJO tends to trigger greater and more frequent extreme rainfall over the land areas along the eastward propagation track (Supplementary Figs. 14, 15), but with regional differences and asymmetric MJO phase changes (Fig. 2a–d). In the Maritime Continent, a transition in the peak of rainfall extremes from the historical level of 30 mm at phase 3 to the level of 50 mm at phases 2–3 is projected, with an associated amplification of MJO activity mainly at phase 2 (Fig. 2a). Such a forward transition implies that the early arrival of the MJO can also be found in the strengthened MJO teleconnection in Pacific-North America regions[17]. The symmetric changes associated with MJO phases likely to be forced by the warming of the eastern Pacific sea surface temperature[17,36,38]. While future extreme rainfall could exceed the historical level, even for phases 1 and 5-8 related to
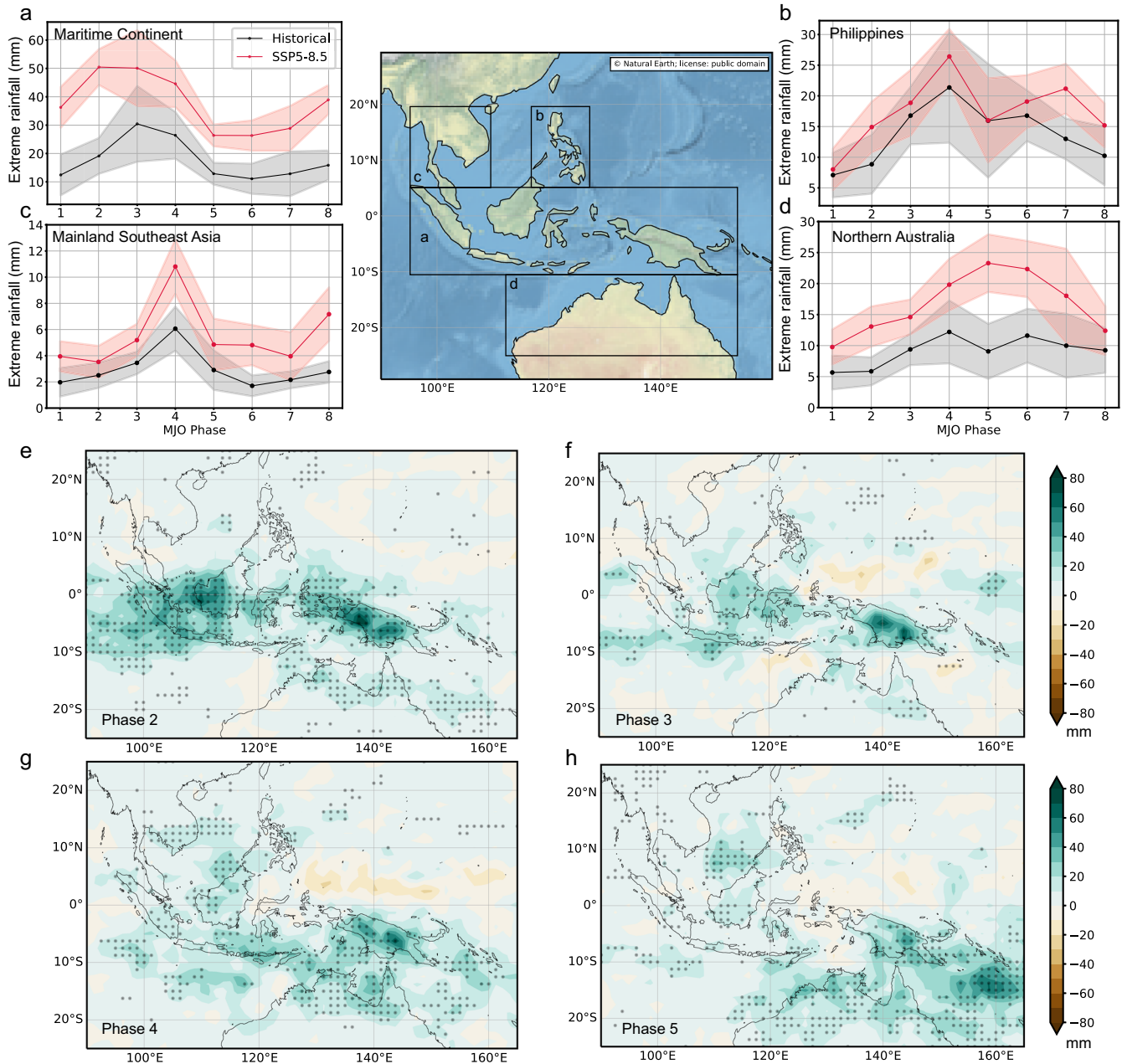
Fig. 2 Projected changes in MJO-induced extreme rainfall at different MJO phases. Land area mean extreme rainfall at phases 1-8 during the future period (2079–2099) and the present period (2015–2035) under the SSP5-8.5 scenario over the Maritime Continent (**a**, 10°S–5°N, 95°E–150°E), the Philippines (**b**, 5°N–20°N, 117°E–125°E), Mainland Southeast Asia (**c**, 5°S–20°N, 95°E–110°E), and northern Australia (**d**, 25°S–10°S, 113°E–155°E). Boundaries of the four sub-regions are while the color shows insert map. Spatial distribution of the changes in MJO-induced extreme rainfall between the future period and the historical period at MJO phase 2 (**e**), phase 3 (**f**), phase 4 (**g**), and phase 5 (**h**) over the study area.

the drier conditions, these changes would still be lower than the averaged extreme rainfall during the entire MJO cycle (Fig. 2a). The extensive increase of extreme rainfall during phases 2–3 is distributed over the west of the Maritime Continent (especially the Kalimantan Island and Java Island) and moves eastwards during phases 2–4 over the east of the New Guinea (Fig. 2e, f). Similarly, in the Philippines, amplification of the MJO-induced extreme rainfall is simulated, accompanied by a phase transition and changes of MJO activity at phases 4 and 7 (Fig. 2b, g, h). In Mainland Southeast Asia, the projected rainfall variability nearly matches the historical variability; and the largest increase is found in phase 4 (Fig. 2c). In northern Australia, the extensive increase of extreme rainfall (from 9.1 to 23 mm) is related to enhanced MJO activity in

phase 5 (Fig. 2d, h). Overall, geographical variations in predicted MJO-induced extreme rainfall changes will develop with warming, in tandem with the asymmetric MJO phase changes, particularly increases in amplitude during phases 2–5.

It is plausible that elevated terrain within the Maritime Continent may block the eastward propagation of MJO by reducing evaporation and enhancing friction[39,40]. The land-sea contrast could thus amplify convergence and vertical motion, leading to the generation of MJO-induced extreme rainfall[39]. The simulated changes in warming-induced asymmetric MJO intensification combined with the elevated terrain tend to produce more extreme rainfall over land areas, especially in Indonesia, Malaysia, Papua New Guinea, and northern Australia (Fig. 2e–g). Another
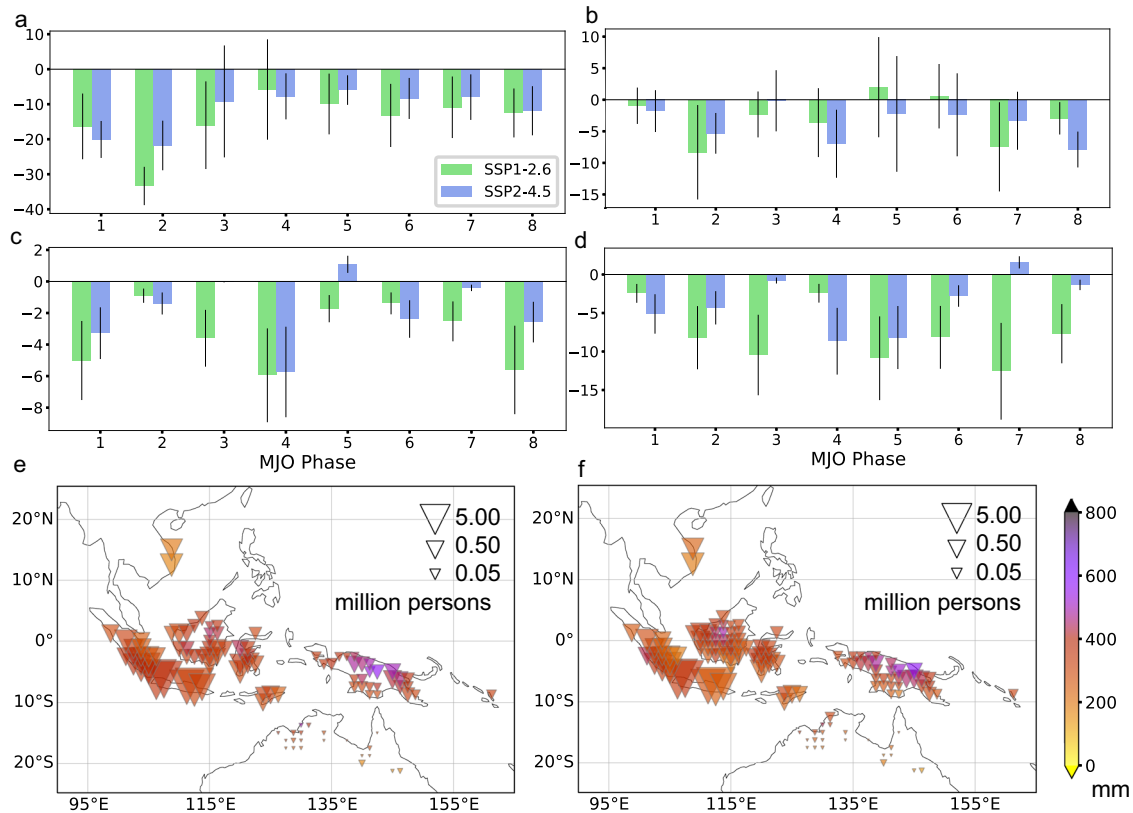
Fig. 3 Effects of global climate mitigations on MJO-induced extreme rainfall and exposed population. Reduction of changes between future (2079-2099) and present (2015-2035) in MJO-induced extreme rainfall at each MJO phase under the SSP1-2.6 and SSP2-4.5 scenarios relative to the SSP5-8.5 scenario over the Maritime Continent (**a**), the Philippines (**b**), Mainland Southeast Asia (**c**), and northern Australia (**d**). Error bars indicate 0.5 times inter-model standard deviation. Decreases in the exposed population to the projected MJO-induced extreme rainfall under the SSP2-4.5 (**e**) and SSP1-2.6 (**f**) scenarios. The exposure of population is estimated for the extreme rainfall threshold taken as the 5-year return value exceedances. The size and color of inverted triangles represent the amount of exposed population and the decreased amount of MJO-induced extreme rainfall, respectively.

noticeable change is the projected extreme rainfall increases in the northeast of Australia over the sea during phases 5–6 (Supplementary Figs. 14, 15), suggesting an amplified MJO in the future may overcome the established barrier effect[41,42].

Climate mitigation constrains MJO-induced consequences

The projected changes in the occurrence and amplitude under the SSP2-4.5 scenario are less compared with those of SSP5-8.5. Additionally, insignificant and even negative trends of MJO strength are projected with the SSP1-2.6 scenario (Supplementary Fig. 16). As a result of constraining future warming, the projected changes in MJO-induced extreme rainfall would also be limited to a lower level (29% for SSP2-4.5 and 11% for SSP1-2.6, compared with 88% for SSP5-8.5; Supplementary Table 3). Considerable reduction of the MJO-induced extreme rainfall increments is consistent, while discrepancies are observed among different MJO phases. Substantial reduction is found in the Maritime Continent for nearly all MJO phases, especially for phase 2, which would experience the most amplified MJO activity (Fig. 3a). Similarly, the increment of MJO-induced extreme rainfall is significantly reduced for phase 4 in the Philippines and Mainland Southeast Asia, and phases 5–8 in northern Australia (Fig. 3b–d). The constrained warming would effectively reduce the extreme rainfall in the area, including MJO-induced extremes.

With the decreases in MJO-induced extreme rainfall being substantial under the SSP2-4.5 scenario, a profound reduction in exposure of population and urban areas is anticipated. Based on a 5-year return value exceedance, only 4.85 million people and 0.12 km² urban area in the region would be exposed, reduced by 95

and 99% relative to the SSP5-8.5 scenario, respectively (Supplementary Table 4). However, the reduction is limited in northern Australia because the exposed population still accounts for 67% of that under SSP5-8.5, and nearly no reduction is found for urban areas (Supplementary Table 4). The reductions in population exposure, as well as the associated urban area exposure, are mainly distributed over Maritime Continent, especially in the Java Island and Sumatera Island, Indonesia (Fig. 3e; Supplementary Fig. 17a). In contrast, in the Philippines, the populations and urban areas exposed to the extreme rainfall exceed the 2-year return value increase, emphasizing different spatial patterns of the extreme rainfall enhancement under the two scenarios (Supplementary Fig. 8c, d).

By constraining warming, in line with the SSP1-2.6 scenario, the exposure to extreme rainfall exceeding a 5-year return value can be almost neglected. No exposure to extremes is expected in the Philippines, mainland Southeast Asia, and northern Australia. An exception occurs in Papua New Guinea of the Maritime Continent, where 0.71 million people and 0.04 million km² of urban areas are exposed. Taking the 2-year return exceedance value as the threshold, the exposure is even smaller than the historical exposure except for Maritime Continent, reinforcing the heterogonous change in the spatial pattern of extremes (Supplementary Fig. 8e, f). Nevertheless, the increased risk for most of the exposed population (urban area) in the Maritime Continent remains high at ~98% (97%) for the SSP1-2.6 scenario. Therefore, such a slight reduction in exposed population and urban area to some extent do not meet the substantial decreases in MJO-induced extreme rainfall. Thus, proactive extreme rainfall impact mitigation

strategies will be needed to address increases in hazard exposure in the future.

DISCUSSION

The IPCC AR6 claims medium confidence in the projected intensification of MJO activity and associated changes of rainfall in a warmer climate[3]. The uncertainties primarily originate from the differences among ESMs in the ability to produce a reasonable MJO amplitude and capture a coherent eastward propagation[42]. Model projection is also sensitive to the simulated patterns of sea surface temperature that affect convection and atmospheric stability[43]. By selecting eight CMIP6 models that performed well in simulating the robust eastward-propagating MJO structure and amplitude[24], we find that nearly 60% increases of boreal winter extreme rainfall are expected over the study area under the fossil-fueled development warming future. Around 84% of the increases are contributed by an amplified MJO, stemming from a projected increase of moisture in a warmer atmosphere leading to more efficient MJO convective heating and more vertical moisture advection[22,29,44]. The increments of MJO-induced extreme rainfall dominate over the lands that are mainly concentrated in Kalimantan Island, Java Island, New Guinea, and northern Australia. This shift is controlled by asymmetric MJO phase changes (magnification mainly in phases 2 and 5 that favor convection), as influenced by distinct contrasts in land and sea in this area. As a result, predicted increases of MJO-induced extreme rainfall that exceed a 5-year return period are predicted in areas currently hosting 96.68 million people, or 9.72 million km^2 of urban lands.

It is known that some ESMs may underestimate MJO amplitude and the MJO-induced precipitation variability[37,45]. Although the representation of the main characteristics of MJO has been largely improved in the CMIP6 models[24], and a rigorous procedure was used in this study to select models with robust eastward-propagating structure, underestimation of MJO may still exists. For instance, the majority of models have difficulties in realistically generating extreme precipitation[6]. Most models used in this study performed well in representing boreal winter total rainfall, but show considerable underestimation for the extremes (Supplementary Fig. 3). For the MJO-related rainfall amounts, the models overestimate 20–30% of the portion of MJO-induced total rainfall, while the overestimation is milder for MJO-induced extreme rainfall. The differences in the portion of MJO-induced extreme rainfall between simulation and observation ranges slightly from −2 to 17% (Supplementary Table 3). Besides, the model underestimates the total extreme rainfall, and the biases may hinder the understanding of future changes in extreme rainfall. Such model biases are likely to be associated with the varying thresholds of 95th extreme rainfall between the simulations and the observations. Despite uncertainties, MJO-related rainfall is likely to produce rainfall extremes that may translate into flood and storm hazards in a warmer climate. Furthermore, to verify whether the threshold that defines MJO active days may be subject to uncertainty, we tested the results by sorting MJO days within three amplitude intervals (Supplementary Fig. 3). The patterns of projected changes in MJO-induced extreme rainfall amount and frequency are generally robust to different thresholds considered, with extreme rainfall increases dominating over the lands of the Maritime Continent and northern Australia (Supplementary Figs. 18, 19). The higher amplitude of MJO events is likely to trigger more intense extreme rainfall, consistent with findings of previous studies[14,15,46].

Beyond tropical Asia and Oceania, the MJO is recognized as a prominent driver in affecting the global climate through teleconnections[47]. Some studies have suggested a strengthened influence of a magnified MJO in higher latitudes in the future[17,18], while others argued that MJO-associated circulation will be suppressed by warming, adding uncertainty to the plausible effect on the MJO outside the tropics[22,29]. As MJO changes are projected to vary among phases, the far-reaching impacts of the MJO fingerprint on circulation and extreme weather could also vary accordingly. For example, a strengthened MJO in phase 5 may contribute to more severe droughts in California (USA) and eastern Africa, while greater wetness would occur for strengthened phase 1 (refs. [12,48]). Hence, further studies are needed to explore projected changes of MJO impacts on various other regions. In addition, during boreal summer, MJO can affect extratropical regions with a northward propagation into monsoon Asia, affecting what is known as the boreal summer intra-seasonal oscillation (BSISO)[49]. However, the multi-model ensemble fails to capture the main pattern of BSISO (see discussions in "Methods"). Future efforts to better represent MJO and BSISO structures are desirable in ESM simulations. Additionally, the projected asymmetric changes in MJO phases that favor convection call for further improvements in the capability and potential of MJO simulation skills, which are critical issues for intra-seasonal to seasonal (S2S) predictions[50,51].

In conclusion, despite uncertainties, our study demonstrates that understanding the MJO phase characteristic changes and the associated extreme rainfall increments is a key issue for several highly populated areas in the Maritime Continent. The comparison of three warming scenarios demonstrates the potential for global warming mitigation in limiting the substantial projected increases of MJO-induced extreme rainfall. Further, we find that lowering the future warming according to the SSP2-4.5 (following the historical trend of development) and SSP1-2.6 (taking the green road) scenarios, can potentially minimize the increases in MJO-induced extreme rainfall and the socio-economic consequences associated with the higher risk.

METHODS

CMIP6 outputs

Historical simulations and ScenarioMIP experiments of eight ESMs from the latest CMIP6 archives[52] were used in this study to assess the MJO contribution to regional extreme rainfall under various scenarios (Supplementary Table 1): (1) BCC-CSM2-MR, (2) CESM2-WACCM, (3) EC-Earth3, (4) EC-Earth3-Veg, (5) GFDL-CM4, (6) MIROC6, (7) MRI-ESM2-0, and (8) NESM3. A single member with the variant label of r1i1p1f1 was chosen for each model to ensure fairness and to limit our data-processing cost[27]. The eight CMIP6 models were selected because of their capability in reproducing a robust eastward-propagating structure when MJO moves across the Maritime Continent in the historical simulations, simultaneously with the MC propagation metric value between 0.8 and 1.0 (ref. [24]). As proposed by Ahn et al. (ref. [24]), the MC propagation metric was calculated as the anomalous intra-seasonal precipitation relative to the Indian Ocean precipitation climatology, to quantify the robustness of MJO propagation over the Maritime Continent.

The historical simulation during 1994–2014 is referred to as the 'historical period'; and the periods of 2015–2035 and 2079–2099 under different scenarios are defined to represent the 'present period' and 'future period', respectively. Three scenarios in the ScenarioMIP experiments were applied: the high emission scenario SSP5-8.5, the medium emission pathway scenario SSP2-4.5, and the green road scenario SSP1-2.6 (ref. [53]).

Because the grid spacing of the eight models is different, we interpolated the model outputs into a common grid of 1.25° (latitude) × 1.25° (longitude) by using linear interpolation. Our study focuses on tropical Southeast Asia and Australia, where MJO-related rainfall is often reported. We compared the changes of MJO-induced precipitation and their potential impact on the population and urban areas over four sub-regions where the impact of MJO has various influence levels during the MJO life cycle (Supplementary Fig. 1). The four sub-regions are: the Maritime Continent (Peninsular Malaysia, Indonesian Archipelago, and Papua New Guinea), the Philippines, Mainland Southeast Asia (Thailand, Cambodia, Laos, Vietnam, southern Myanmar), and northern Australia. The relative analyses during the historical, present, and future periods were performed for the boreal winter (November–April), when the MJO is the most active.

Reference data

The NCEP-DOE Reanalysis 2 (ref. [54]) and NOAA Interpolated Outgoing Longwave Radiation[55] products/datasets were used to explore the reference MJO structures over the study area during a representative historical period of 1979–2001 (ref. [10]). Daily precipitation data retrieved from the Global Precipitation Climatology Center (GPCC)[56] was treated as the reference to validate the overall performance of the precipitation simulations of CMIP6 models. The GPCC data was interpolated into the 1.25° × 1.25° grid to match the CMIP6 model outputs. The land mask data on an original 0.25° × 0.25° spatial resolution from the NOAA High-resolution Blended Analysis[57] was used to define land areas. The land mask data was first classified into two categories: ocean with the pixel value of 0 and land with the value of 1. Then the original land mask data was aggregated into the 1.25° × 1.25° grid to match the CMIP6 models and validation data. Lastly, the fraction of land weight in each grid was computed by dividing the number of 0.25° × 0.25° land pixels by the total number of pixels within the grid. The land weight value of 0 indicates that the grid contains no land, and was excluded from the regional analyses. The simulated precipitation results of CMIP6 models are spatially averaged over the remaining grids and weighted by their land-weight fractions to obtain the precipitation on land for each experiment during the study periods.

MJO RMM index

The real-time MJO multivariate (RMM) index created by Wheeler & Hendon (ref. [10]) was adopted to quantify the amplitude of MJO convective states and the locations of convection centers for the reanalysis data and the selected models in this study. First, the combined empirical orthogonal functions (CEOF) analyses were employed for three key variables, namely, outgoing longwave radiation (OLR), 850 hPa zonal winds (U850), and 250-hPa zonal winds (U250) by following the calculation steps recommended by the US Climate Variability and Predictability (CLVAR) MJO Working Group: (1) daily anomalies of the three variables were extracted and calculated, and the 201-point Lanczos filter method was applied to filter the daily anomalies to construct intra-seasonal anomalies; (2) the CEOF analyses were carried out by using the filtered anomalies of the OLR, U850, and U250; (3) the first two leading modes of MJO CEOF analyses were obtained based on their percentage variances that were generated using the anomalies of three variables over 15°S–15°N. For the MJO structures during the representative historical period, the reference EOFs (i.e., EOF1 and EOF2) in the study area were calculated with the above procedures by using the U850, U250 from the NCEP-DOE Reanalysis 2 datasets, and OLR from the NOAA Interpolated Outgoing Longwave Radiation. For the historical simulations and ScenarioMIP experiments of the eight CMIP6 models, the EOFs were calculated using available model output variables. The explained variances of the first two leading modes and the percentage variances of the three variables for the reference EOFs and the selected CMIP6 models EOFs during the historical period are given in Supplementary Table 2. The eight models generally captured the MJO propagation patterns, despite somewhat underestimating the observed metric. Furthermore, the zonal MJO structures of the two leading EOFs derived from the models during the historical period compare well with those from the reanalysis observations (Supplementary Fig. 2), implying the overall accuracy of the simulations of MJO in the study area.

OLR, U850, and U250 anomalies for each selected model were further projected onto the reference EOFs to construct the corresponding principal components RMM$_1$ and RMM$_2$ on a daily scale (ref. [10]). This standardized approach enables consistent comparison among different models. Specifically, the MJO amplitude was computed as $\sqrt{RMM_1^2 + RMM_2^2}$. Days, when the MJO amplitude was larger than 1, were identified as MJO active days. They were further classified into eight groups based on their MJO phase values estimated by $\tan^{-1}$ (RMM$_2$/RMM$_1$). In the schematic diagram of the RMM index, each phase covers half of the quadrant, starting counterclockwise with the MJO phase 5 in the first half quadrant (Supplementary Fig. 3). A whole MJO life cycle contains eight phases, which correspond to longitudinal locations of convection centers propagating from the Indian Ocean to the Western Pacific, with a latitudinal extent of about 15° north and south of the equator (Supplementary Figs. 1 and 3). MJO occurrence days were defined as the number of MJO active days during the boreal winter season. To address long-term (85 years during 2015–2099) changes of MJO structures in the CMIP6 ScenarioMIP experiments, the trends of MJO occurrence days and amplitude were calculated based on the multi-model mean time series using linear regression under the three scenarios. (Supplementary Figs. 12, 13).

Precipitation analysis

In the historical, present, and future periods for the eight selected CMIP6 models, total rainfall amount (mm) was defined as the accumulated precipitation amount during the boreal winter for each year. The extreme rainfall amount (mm) was determined as the multi-season average of the precipitation amount that exceeds the extreme threshold. For each 1.25° × 1.25° grid point, the threshold used to distinguish extreme precipitation was defined as the 95th percentile of daily precipitation on wet days (daily precipitation is larger than 1.0 mm) during the boreal winter in the historical period. In addition, we analyzed the extreme rainfall frequency (%), defined as the ratio of the number of days with extreme precipitation to the total days during boreal winter. The performance of the selected CMIP6 models was evaluated by comparing the historical boreal winter total rainfall and extreme rainfall with the GPCC observations over the study area. Generally, models successfully modeled the longitudinal and latitudinal variation of total rainfall amount (Supplementary Fig. 4a), implying an overall good skill of all simulations. As for extreme rainfall, all models captured similar spatial fluctuations as those observed, but the multi-model median value is underestimated (Supplementary Fig. 4b).

The MJO-induced rainfall amount and extreme rainfall amount/frequency were accounted with a 6-day lag of MJO active days, for the reason that the effect of MJO on climate can be delayed by a few days[11,17]. The proportion of MJO-induced rainfall was computed by summing up the rainfall occurring 6 days after the MJO active day across the year then divided by the total rainfall. This ratio is referred to as the contribution of MJO (%). Note that in this study, the total rainfall was calculated during the boreal winter for each year. Similarly, the contribution of MJO-induced extreme rainfall was the proportion of MJO-induced extreme rainfall to the total extreme rainfall. The MJO-induced rainfall was further divided and assigned to phases 1–8 based on the MJO-phase-composited fields. Multi-model mean MJO-phase-composite precipitation anomaly and the MJO-phase-composite extreme rainfall frequency illustrated the changes in spatial patterns among the phases within the MJO life cycle, displaying a clear eastward propagation structure of MJO during the historical period (Supplementary Figs. 5, 6). Compared with GPCC observations, the selected CMIP6 models accurately simulated the variability of MJO-phase-composite precipitation anomaly over the four sub-regions in the study area (Supplementary Fig. 7). These results demonstrated the models' ability to capture the structures of the MJO life cycle and MJO-induced precipitation. To investigate how various warming pathways affect the characteristics of MJO-induced rainfall and the contribution of MJO events to regional extremes, we use the changes of rainfall variables as the multi-model median differences of the simulated precipitation between the future period (2079–2099) under various scenarios and the present period (2015–2035) to eliminate any systematic biases due to different forcings that different models used in their historical and ScenarioMIP experiments. Therefore, the projected future rainfall variables in different scenarios are computed by adding up these future-present differences to the historical level.

Exposure of population or urban area under different scenarios

Exposure is defined as the estimated population and urban areas that suffers from projected future MJO-induced extreme rainfall exceeding the threshold that may cause rain-induced hazards, at a 1.25° × 1.25° grid boxes[58]. The drainage system of local infrastructure is usually designed to tolerate rainfall events of a 5-year return level in Southeast Asia, yet lack of adequate maintenance might limit its reliability[46,59,60]. Thus, two thresholds are chosen to satisfy the 2- and 5-year return levels which are derived from the 1964–2014 extreme rainfall for boreal winter seasons[46]. Following ref. [58], the extreme return levels are calculated in two steps: (1) Fit the generalized extreme value (GEV) distribution with 1964–2014 extreme rainfall with the maximum likelihood algorithm to obtain the three GEV parameters representing the location, the scale, and the shape parameter of the distribution. The three parameters are then smoothed spatially with a filter involving 3 × 3 grids. (2) Passing the smoothed parameters to the inverted GEV distribution to calculate the 2-year and 5-year return levels which correspond to a probability of 50 and 20%, respectively.

The population count data at 1° resolution is from Gridded Population of the World (GPW), version 4.11 for the year 2015 (ref. [61]), and has further been interpolated to a grid of 1.25°. The urban area is obtained from a satellite-based high resolution (30 m) global urban map for the year 2015 (ref. [62]). The exposure of urban areas to extreme rainfall is calculated by aggregating the value of all urban pixels within each 1.25° × 1.25° grid.

Here, the population and urban area exposures under all scenarios are estimated based on their current state (i.e., the year 2015). Considering future population growth and urbanization, our estimated exposure to a warmer climate would be a more conservative one. It is worthy of note that the result of zero exposure under the 5-year return value exceedance in the Philippines and Mainland Southeast Asia is due to the fact that our selected months from November to April correspond to the local dry season while the thresholds of extreme rainfall are relative to the entire year.

We compare the distribution of exposed population and urban areas between these thresholds (Supplementary Figs. 12 and 17). If taking the exceedance of 2-year return values as threshold, the future extreme rainfall in most of the study regions will exceed this threshold. Noted that for historical extreme rainfall, the exposed population is 186.80 million, and exposed urban area is 18.59 km^2 (Supplementary Table 4), implying that the extreme rainfall could exceed the 2-year return values commonly. Thus, proactive extreme rainfall impact mitigation strategies will be needed to address increases in hazard exposure in the future.

BSISO index

Different from the MJO, which is dominant during the boreal winter, the boreal summer intra-seasonal oscillation (BSISO)[63,64], is the intra-seasonal tropical climate variability during the boreal summer (May–October). For Mainland Southeast Asia and the Philippines, where seasonal mean rainfall is larger during the boreal summer months, BSISO serves as the most dominant source in modulating rainfall and extreme rainfall[44]. BSISO shows more complex structures than MJO due to the coexistence of eastward and northward propagating. We constructed the BSISO indices using NCEP-DOE Reanalysis 2 and NOAA Interpolated Outgoing Longwave datasets[55,56] during a representative period of 1981–2010 following the procedure described in ref. [44]. The BSISO indices for the historical simulations of the eight CMIP6 models were also calculated for the same period. Generally, the BSISO1 phase composite presents a canonical northward propagating pattern, while the BSISO2 phase composite shows a northward and northwestward propagating pattern (Supplementary Figs. 20, 21). However, the multi-model ensemble fails to capture the main propagating pattern of BSISO, and the magnitude was largely underestimated (Supplementary Figs. 22, 23). Future efforts to better represent BSISO structures are clearly desirable.

DATA AVAILABILITY

Model output from CMIP6 is publicly available at https://esgf-node.llnl.gov/projects/cmip6/. Precipitation data from GPCC are publicly available at https://psl.noaa.gov/data/gridded/data.gpcc.html. The NCEP-DOE Reanalysis 2 data is publicly available at https://psl.noaa.gov/data/gridded/data.ncep.reanalysis2.html. The NOAA Interpolated Outgoing Longwave Radiation data is publicly available at https://psl.noaa.gov/data/gridded/data.interp_OLR.html. The land mask data is publicly available at https://psl.noaa.gov/data/gridded/data.noaa.oisst.v2.highres.html. The global urban map dataset is publicly available at https://doi.org/10.6084/m9.figshare.11513178.v1. Population distributions (GPWv4.11, ref. [65]) are publicly available at https://sedac.ciesin.columbia.edu/data/set/gpw-v4-population-count-rev11.

CODE AVAILABILITY

The data in this study was analyzed and the figures were created with Python. All relevant codes used in this work are available on request from the corresponding author Z. Zeng.

REFERENCES

1. CRED, UNDRR. Human Cost of Disasters. An overview of the last 20 years: 2000–2019. https://reliefweb.int/report/world/human-cost-disasters-overview-last-20-years-2000-2019 (2020).
2. Global Catastrophe Recap. December 2020. Aon Benfield Analytics. Retrieved April 25, 2021. http://thoughtleadership.aon.com/Documents/20210012-analytics-if-september-global-recap.pdf (2020).
3. IPCC. *Contribution of Working Group I to the Sixth Assessment Report of the Intergovernmental Panel on Climate Change* (Cambridge, 2021).
4. O'Gorman, P. A. & Schneider, T. The physical basis for increases in precipitation extremes in simulations of 21st-century climate change. *Proc. Natl Acad. Sci. USA* **16**, 14773–14777 (2009).
5. Donat, M., Lowry, A., Alexander, L., O'Gorman, P. A. & Maher, N. More extreme precipitation in the world's dry and wet regions. *Nat. Clim. Change* **6**, 508–513 (2016).
6. Chen, H., Sun, J., Lin, W. & Xu, H. Comparison of CMIP6 and CMIP5 models in simulating climate extremes. *Sci. Bull.* **65**, 1415–1418 (2020).
7. Rogelj, J. et al. Understanding the origin of Paris Agreement emission uncertainties. *Nat. Commun.* **8**, 15748 (2017).
8. Tellman, B. et al. Satellite imaging reveals increased proportion of population exposed to floods. *Nature* **596**, 80–86 (2021).
9. Madden, R. A. & Julian, P. R. Detection of a 40–50 day oscillation in the zonal wind in the tropical pacific. *J. Atmos. Sci.* **28**, 702–708 (1971).
10. Wheeler, M. C. & Hendon, H. H. An all-season real-time multivariate MJO index: Development of an index for monitoring and prediction. *Mon. Weath. Rev.* **132**, 1917–1932 (2004).
11. Zhang, C. Madden–Julian Oscillation: Bridging weather and climate. *Bull. Am. Meteorol. Soc.* **94**, 1849–1870 (2013).
12. Roxy, M. K. et al. Twofold expansion of the Indo-Pacific warm pool warps the MJO life cycle. *Nature* **575**, 647–651 (2019).
13. Bui, H. X. & Maloney, E. D. Changes in Madden–Julian Oscillation precipitation and wind variance under global warming. *Geophys. Res. Lett.* **45**, 7148–7155 (2018).
14. Jones, C. & Carvalho, L. M. V. Changes in the activity of the Madden–Julian Oscillation during 1958–2004. *J. Clim.* **19**, 6353–6370 (2006).
15. Xavier, P., Rahmat, R., Cheong, W. K. & Wallace, E. Influence of Madden–Julian Oscillation on Southeast Asia rainfall extremes: Observations and predictability. *Geophys. Res. Lett.* **41**, 4406–4412 (2014).
16. Hand, E. The storm king. *Science* **350**, 22–25 (2015).
17. Zhou, W., Yang, D., Xie, S. -P. & Ma, J. Amplified Madden–Julian Oscillation impacts in the Pacific-North America region. *Nat. Clim. Change* **20**, 654–660 (2020).
18. Samarasinghe, S. M., Connolly, C., Barnes, E. A., Ebert-Uphoff, I. & Sun, L. Strengthened causal connections between the MJO and the North Atlantic with climate warming. *Geophys. Res. Lett.* **48**, e2020GL091168 (2021).
19. Arnold, N. P., Branson, M., Kuang, Z., Randall, D. A. & Tziperman, E. MJO Intensificarion with warming in the superparameterized CESM. *J. Clim.* **28**, 2706–2724 (2015).
20. Adames, Á. F., Kim, D., Sobel, A. H., Del Genio, A. & Wu, J. Changes in the structure and propagation of the MJO with increasing CO_2. *J. Adv. Model. Earth Syst.* **9**, 1251–1268 (2017).
21. Chang, C.-W. J., Tseng, W.-L., Hsu, H.-H., Keenlyside, N. & Tsuang, B.-J. The Madden–Julian Oscillation in a warmer world. *Geophys. Res. Lett.* **42**, 6034–6042 (2015).
22. Maloney, E. D., Adames, Á. F. & Biu, H. Madden–Julian Oscillation changes under anthropogenic warming. *Nat. Clim. Change* **9**, 26–33 (2019).
23. IPCC. *Contribution of Working Group I to the Fifth Assessment Report of the Intergovernmental Panel on Climate Change* (Cambridge, 2013).
24. Ahn, M. S. et al. MJO propagation across the Maritime Continent: Are CMIP6 models better than CMIP5 models? *Geophys. Res. Lett.* **47**, e2020GL087250 (2020).
25. Hirsch, R. & Archfield, S. Not higher but more often. *Nat. Clim. Change* **5**, 198–199 (2015).
26. Mallakpour, I. & Villarini, G. The changing nature of flooding across the central United States. *Nat. Clim. Change* **5**, 250–254 (2015).
27. Bui, H. & Maloney, E. D. Transient response of MJO precipitation and circulation to Greenhouse Gas Forcing. *Geophys. Res. Letts.* **46**, 13546–13555 (2019).
28. Tierolf, L., Moel, H. & Vliet, J. Modeling urban development and its exposure to river flood risk in Southeast Asia. *Comp. Environ. Urban. Syst.* **87**, 101620 (2021).
29. Oliver, E. C. & Thompson, K. R. A reconstruction of Madden–Julian Oscillation variability from 1905 to 2008. *J. Clim.* **25**, 1996–2019 (2012).
30. Carlson, H. & Caballero, R. Enhanced MJO and transition to super rotation in warm climates. *J. Adv. Model. Earth Syst.* **8**, 304–318 (2016).
31. Wolding, B. O., Maloney, E. D., Henderson, S. A. & Branson, M. Climate change and the Madden–Julian Oscillation: A vertically resolved weak temperature gradient analysis 307–331. *J. Adv. Model. Earth Syst.* **9**, 307–331 (2017).
32. Jones, C. & Carvalho, L. M. V. Will global warming modify the activity of the Madden–Julian Oscillation? *Q. J. R. Meteorol. Soc.* **137**, 544–552 (2010).
33. Holloway, C. E. & Neelin, J. D. Moisture vertical structure, column water vapor, and tropical deep convection. *J. Atmos. Sci.* **66**, 1665–1683 (2009).
34. Arnold, N. P., Kuang, Z. & Tziperman, E. Enhanced MJO-like variability at high SST. *J. Clim.* **26**, 988–1001 (2013).

35. Yoo, C., Feldstein, S. & Lee, S. The impact of the Madden–Julian Oscillation trend on the Arctic amplification of surface air temperature during the 1979–2008 boreal winter. *Geophys. Res. Lett.* **38**, L24804 (2011).

36. Song, E. J. & Seo, K. H. Past- and present-day Madden–Julian Oscillation in CNRM-CM5. *Geophys. Res. Lett.* **43**, 4042–4048 (2016).

37. Zhang, C., Adames, Á. F., Khouider, B., Wang, B. & Yang, D. Four theories of the Madden–Julian Oscillation. *Rev. Geophys.* **58**, e2019RG000685 (2020).

38. Subramanian, A. et al. The MJO and global warming: A study in CCSM4. *Clim. Dyn.* **42**, 2019–2031 (2014).

39. Hsu, H. & Lee, M. Topographic effects on the eastward propagation and initiation of the Madden–Julian Oscillation. *J. Clim.* **15**, 795–809 (2005).

40. Zhang, C. & Ling, J. Barrier effect of the Indo-Pacific Maritime Continent on the MJO: Perspectives from tracking MJO precipitation. *J. Clim.* **30**, 3439–3459 (2017).

41. Chen, G., Ling, J., Li, C., Zhang, Y. & Zhang, C. Barrier effect of the Indo-Pacific Maritime Continent on MJO propagation in observations and CMIP5 Models. *J. Clim.* **33**, 5173–5193 (2020).

42. Ahn, M. S. et al. MJO simulation in CMIP5 climate models: MJO skill metrics and process-oriented diagnosis. *Clim. Dyn.* **49**, 4023–4045 (2017).

43. Maloney, E. D. & Xie, S.-P. Sensitivity of MJO activity to the pattern of climate warming. *J. Adv. Model. Earth Syst.* **5**, 32–47 (2013).

44. Adames, Á. F., Kim, D., Sobel, A. H., Del Genio, A. & Wu, J. Characterization of moist processes associated with changes in the propagation of the MJO with increasing CO_2. *J. Adv. Model. Earth Syst.* **9**, 2946–2967 (2017).

45. Le, P. V. V., Guilloteau, C., Mamalakis, A. & Foufoula-Georgiou, E. Underestimated MJO variability in CMIP6 models. *Geophys. Res. Lett.* **48**, e2020GL092244 (2021).

46. Schreck, C. J. III Global survey of the MJO and extreme precipitation. *Geophys. Res. Lett.* **48**, e2021GL094691 (2021).

47. Chen, G. Diversity of the global teleconnections associated with the Madden–Julian Oscillation. *J. Clim.* **34**, 397–413 (2021).

48. Yoo, C., Lee, S. & Feldstein, S. B. Mechanisms of Arctic surface air temperature change in response to the Madden–Julian Oscillation. *J. Clim.* **25**, 5777–5790 (2012).

49. Lee, J. Y. et al. Real-time multivariate indices for the boreal summer intraseasonal oscillation over the Asian summer monsoon region. *Clim. Dyn.* **40**, 493–509 (2013).

50. Meehl, G. A. et al. Initialized Earth System prediction from subseasonal to decadal timescales. *Nat. Rev. Earth Environ.* **2**, 340–357 (2021).

51. Xiang, B. Q. et al. S2S Prediction in GFDL SPEAR: MJO diversity and teleconnections. *Bull. Am. Meteorol. Soc.* https://doi.org/10.1175/BAMS-D-21-0124.1 (2021).

52. Eyring, V. et al. Overview of the Coupled Model Intercomparison Project Phase 6 (CMIP6) experimental design and organization. *Geosci. Model Dev.* **9**, 1937–1958 (2016).

53. O'Neil, B. C. et al. The Scenario Model Intercomparison Project (ScenarioMIP) for CMIP6. *Geosci. Model Rev.* **9**, 3461–3482 (2016).

54. Kanamitsu, M. et al. NCEP–DOE AMIP-II reanalysis (R-2). *Bull. Am. Meteorol. Soc.* **83**, 1631–1644 (2002).

55. Liebmann, B. & Smith, C. A. Description of a complete (interpolated) outgoing longwave radiation dataset. *Bull. Am. Meteorol. Soc.* **77**, 1275–1277 (1996).

56. Schamm, K. et al. GPCC Full Data Daily Version 2020 at 1.0°: Daily Land Surface Precipitation from Rain-Gauges built on GTS-based and Historical Data. Retrieved August 12, 2022. https://doi.org/10.5065/D6V69GRT (2020).

57. Reynolds, W. R. et al. Daily high resolution-blended analyses for sea surface temperature. *J. Clim.* **20**, 5473–5496 (2007).

58. Zhang, W., Zhou, T., Zou, L., Zhang, L. & Chen, X. Reduced exposure to extreme precipitation from 0.5 °C less warming in global land monsoon regions. *Nat. Commun.* **9**, 3153 (2018).

59. Chang, C. H. Preparedness and storm hazards in a global warming world: Lessons from Southeast Asia. *Nat. Hazards* **56**, 667–679 (2011).

60. Liew, S. C., Raghavan, S. V. & Liong, S. Y. Development of Intensity-Duration-Frequency curves at ungauged sites: Risk management under changing climate. *Geosci. Lett.* **1**, 8 (2014).

61. Center for International Earth Science Information Network–CIESIN–Columbia University. Gridded Population of the World, Version 4 (GPWv4): Population Count, Revision 11. Palisades, NY: NASA Socioeconomic Data and Applications Center (SEDAC). https://doi.org/10.7927/H4JW8BX5. Accessed 1st July (2021).

62. Liu, X. et al. High-spatiotemporal-resolution mapping of global urban change from 1985 to 2015. *Nat. Sustain.* **3**, 564–570 (2020).

63. Wang, B. & Xie, X. A model for the boreal summer intraseasonal oscillation. *J. Atmos. Sci.* **54**, 72–86 (1997).

64. Jiang, X., Li, T. & Wang, B. Structures and mechanisms of the northward propagating boreal summer intraseasonal oscillation. *J. Clim.* **17**, 1022–1039 (2004).

65. Jones, B. et al. Future population exposure to US heat extremes. *Nat. Clim. Change* **5**, 652–655 (2015).

ACKNOWLEDGEMENTS

AUTHOR CONTRIBUTIONS

Z.Z. designed the research; S.L. performed the analysis; S.L., A.D.Z., and D.W. wrote the draft. All authors contributed to the interpretation of the results and the writing of the paper.

COMPETING INTERESTS

The authors declare no competing interests.

ADDITIONAL INFORMATION

Supplementary information The online version contains supplementary material available at https://doi.org/10.1038/s41612-022-00291-1.

Correspondence and requests for materials should be addressed to Dashan Wang or Zhenzhong Zeng.

Reprints and permission information is available at http://www.nature.com/reprints

Publisher's note Springer Nature remains neutral with regard to jurisdictional claims in published maps and institutional affiliations.